CHAPTER 4

Optimisation-based wavefront sensorless adaptive optics for non-linear microscopy

Jacopo Antonello, Tim van Werkhoven, Michel Verhaegen, Hoa H. Truong, Christoph U. Keller, and Hans C. Gerritsen, *Journal of the Optical Society of America A* (accepted)

Optical aberrations have detrimental effects in multiphoton microscopy. These effects can be curtailed by implementing model-based wavefront sensorless adaptive optics, which only requires the addition of a wavefront shaping device such as a deformable mirror to an existing microscope. The aberration correction is achieved by maximising a suitable image quality metric. We implemented a model-based aberration correction algorithm in a second-harmonic microscope. We remove the tip, tilt and defocus aberrations from the basis functions used for the control of the deformable mirror, as these aberrations induce distortions in the acquired images. We compute the parameters of a quadratic polynomial that is used to model the image quality metric directly from experimental input-output measurements. Finally we apply the aberration correction by maximising the image quality metric using the least-squares estimate of the unknown aberration.

4.1 Introduction

Multiphoton microscopy techniques such as two-photon fluorescence microscopy (Denk et al., 1990) and second-harmonic microscopy (Campagnola et al., 2001) are commonly employed to image biological specimens. Exploiting the image sectioning properties of these processes, one can create high-resolution 3D reconstructions that are invaluable for biomedical research. One limiting factor is the presence of specimen-induced aberrations. Because the index of refraction is not homogeneous within the specimen, aberrations affect both the resolution and the maximum depth of penetration (Booth, 2007a). Using adaptive optics (Tyson, 2010), these detrimental effects can be minimised by reducing the phase aberrations. A phase aberration can be introduced in the excitation beam by means of a deformable mirror, for example. Chosen correctly, such a phase aberration can suppress some amount of the specimen-induced aberrations.

Direct measurement of the specimen-induced aberrations is challenging. One solution involves measuring the aberrations of the excitation light that is back-scattered from the specimen (Rahman & Booth, 2013; van Werkhoven et al., 2014, 2012; Rückel et al., 2006; Cha et al., 2010; Bueno et al., 2010). In this case, the difficulty arises in excluding the light that is reflected from the out-of-focus layers of the specimen (Rahman & Booth, 2013; van Werkhoven et al., 2014). Additionally, these measurements are weakly sensitive to odd aberrations (Rahman & Booth, 2013), due to the double pass effect (Artal et al., 1995b). In another solution, instead, the emission from a point source inside the specimen is used to perform Shack-Hartmann wavefront sensing (Azucena et al., 2010; Aviles-Espinosa et al., 2011; Shaw et al., 2013; Tao et al., 2013b,a). Here the difficulty stems from the lack of such reference point sources within the specimen and from the limited number of photons available in the emission signal.

An alternative, indirect approach involves deducing the specimen-induced aberrations solely by examining the emission signal. This approach only requires the addition of a deformable mirror into the excitation path of an existing microscope. A solution that is based on the segmentation of the pupil has been proposed (Ji et al., 2009; Milkie et al., 2011). Other solutions are based on the optimisation of an image quality metric, which attains its global maximum when the residual aberration is maximally suppressed. In practice, different trial aberrations are sequentially applied with the deformable mirror until the image quality metric attains its maximum.

General optimisation algorithms can be used to maximise the image quality metric (Vdovin, 1998; Albert et al., 2000; Vorontsov, 2002; Marsh et al.,

2003; Murray et al., 2005; Wright et al., 2005). However, because these algorithms have no prior knowledge about the metric, a large number of trial aberrations must be evaluated before the metric is maximised (Booth, 2007a, 2006; Antonello et al., 2012). Reducing the number of trial aberrations is critical in achieving short image acquisition times and in limiting side effects such as photobleaching and phototoxicity. For small aberrations, the response of the image quality metric can be approximated using a simple model, such as a quadratic polynomial (Neil et al., 2000; Booth et al., 2002; Booth, 2006; Débarre et al., 2007; Booth, 2007b; Débarre et al., 2008, 2009; Jesacher et al., 2009; Facomprez et al., 2012; Zeng et al., 2012; Antonello et al., 2012). Model-based aberration correction algorithms (Neil et al., 2000; Booth et al., 2002; Booth, 2006; Débarre et al., 2007; Booth, 2007b; Débarre et al., 2008, 2009; Jesacher et al., 2009; Song et al., 2010; Linhai & Rao, 2011; Yoo et al., 2012; Facomprez et al., 2012; Zeng et al., 2012; Antonello et al., 2012) exploit the knowledge about the model of the metric to quicken the aberration correction, thus curtailing the aforementioned side effects.

In this paper, we investigate applying a model-based wavefront sensorless aberration correction algorithm to a second-harmonic microscope.

The paper is organised as follows. In section 4.2 we discuss the definition of the basis functions for the control of the deformable mirror. In section 4.3 we outline our proposed algorithm for the aberration correction. In section 4.4 we report the experimental results. The conclusions are drawn in section 4.5.

4.2 Definition of the basis functions for the control of the deformable mirror

The basis functions should satisfy two different requirements. The first requirement is that the basis functions be orthogonal to the x-tilt, y-tilt and defocus aberrations. As mentioned in the introduction, these aberrations induce unwanted displacements or distortions to the region of the specimen that is acquired by scanning the focal point (Débarre et al., 2008, 2009; Thayil & Booth, 2011). When using Zernike modes as the basis functions, the unwanted aberrations can be set to zero.

A second requirement is that the basis functions express the capabilities of the deformable mirror in an accurate and concise form, by taking into account the mechanical limitations of the mirror and the misalignment in the optical system as much as possible. This requirement is not satisfied when using Zernike modes as the basis functions since a deformable mir-

ror with N_a actuators cannot accurately induce a set of N_a Zernike modes.

We now discuss a simple procedure to define a new set of basis functions that satisfy the two requirements discussed so far. This procedure is based on the decomposition of a matrix H that approximately describes a linear relationship between the control signals of the deformable mirror and a set of Zernike coefficients. For completeness, we first report how H can be computed from input-output measurements.

Computation of matrix H from input-output measurements

Let N_a be the number of actuators of the deformable mirror. Assuming that the deformable mirror is a linear device, the phase aberration $\Phi(\boldsymbol{\xi})$ is given by the superposition of the influence functions $\psi_i(\boldsymbol{\xi})$ of each actuator, where $\boldsymbol{\xi}$ is the spatial coordinate in the pupil and u_i is the control signal of the i-th actuator

$$\Phi(\boldsymbol{\xi}) = \sum_{i=1}^{N_a} u_i \psi_i(\boldsymbol{\xi}). \tag{4.1}$$

For a suitable number N_z of Zernike modes $\mathcal{Z}_j(\boldsymbol{\xi})$, we have that

$$\Phi(\boldsymbol{\xi}) \approx \sum_{j=2}^{1+N_z} z_j \mathcal{Z}_j(\boldsymbol{\xi}), \tag{4.2}$$

where z_j is the j-th Zernike coefficient. We neglect the piston mode $\mathcal{Z}_1$ since this does not affect the image and assume that $\Phi(\boldsymbol{\xi})$ and $\psi_i(\boldsymbol{\xi})$ have zero mean value over the pupil.

We collect the coefficients u_i and z_j respectively into vectors $\mathbf{u} \in \mathbb{R}^{N_a}$ and $\mathbf{z} \in \mathbb{R}^{N_z}$. By considering a grid defined in the pupil, N_c samples of $\Phi(\boldsymbol{\xi})$ are collected into a vector $\boldsymbol{\phi} \in \mathbb{R}^{N_c}$. Similarly, we evaluate $\psi_i(\boldsymbol{\xi})$ and $\mathcal{Z}_j(\boldsymbol{\xi})$ over the grid and define two matrices $\Psi \in \mathbb{R}^{N_c \times N_a}$ and $Z \in \mathbb{R}^{N_c \times N_z}$. From (4.1) and (4.2) we have that $\boldsymbol{\phi} = \Psi \mathbf{u}$ and $\boldsymbol{\phi} \approx Z\mathbf{z}$.

We would like to recover a matrix H which maps an actuation vector $\mathbf{u}$ into the corresponding vector of Zernike coefficients $\mathbf{z}$, i.e., $\mathbf{z} \approx H\mathbf{u}$. H can be computed using input-output measurements, so that the misalignment in the optical system is accounted for. Using a Shack-Hartmann wavefront sensor or interferometric methods (Wang & Booth, 2009; Fernandez & Artal, 2003; Vdovin et al., 2013; Booth et al., 2005) one can collect a set of measurements of the phase $\boldsymbol{\phi}_1, \dots, \boldsymbol{\phi}_D$ corresponding to different settings of the deformable mirror $\mathbf{u}_1, \dots, \mathbf{u}_D$.

We compute H by minimising the following criterion,

$$\min_H \sum_{i=1}^{D} \|\boldsymbol{\phi}_i - ZH\mathbf{u}_i\|^2. \tag{4.3}$$

Setting the derivative with respect to H to zero, we have the following normal equation

$$Z^T ZH(\sum_{i=1}^{D} \mathbf{u}_i \mathbf{u}_i^T) = Z^T(\sum_{i=1}^{D} \boldsymbol{\phi}_i \mathbf{u}_i^T), \tag{4.4}$$

which can be solved by multiplying from the left and from the right by the inverse matrices of $Z^T Z$ and $\sum_{i=1}^{D} \mathbf{u}_i \mathbf{u}_i^T$. For a properly defined grid, the inverse of $Z^T Z$ exists, since Z is full column rank due to the orthogonality property of the Zernike modes. Additionally, vectors $\mathbf{u}_i$ can be selected so that $\sum_{i=1}^{D} \mathbf{u}_i \mathbf{u}_i^T$ is full rank.

In our system we have that $N_a = 17$ and $N_c = 75912$. We performed $D = 4N_a$ measurements of the phase $\boldsymbol{\phi}_1, \ldots, \boldsymbol{\phi}_{4N_a}$. In each measurement, a single actuator is poked while the other actuators are at rest. We empirically chose $D = 4N_a$, other choices are possible provided $D \geq N_a$. The choice of N_z is more critical. With a poor choice of N_z, the accuracy requirement discussed at the beginning of section 4.2 may not be fulfilled and the approximation $\mathbf{z} \approx H\mathbf{u}$ may be too rough. We chose $N_z = 35$ by evaluating the error in approximating the phase measurements $\boldsymbol{\phi}_i$ using an increasing number of Zernike modes.

SVD-based removal of the x-tilt, y-tilt and defocus aberrations

From the previous section, we conclude that, in our system, the $N_a = 17$ influence functions approximately span a subspace of the space spanned by the first $N_z = 35$ Zernike modes. Because $\text{rank}(H) < N_z$, there exist non zero vectors $\mathbf{z}$ that do not belong to the range of H and the Zernike modes should not be used as the basis functions for the control of the deformable mirror.

We can split vector $\mathbf{z}$ and matrix H so that $\mathbf{z} \approx H\mathbf{u}$ is partitioned as

$$\begin{bmatrix} \mathbf{z}_l \\ \mathbf{z}_h \end{bmatrix} \approx \begin{bmatrix} H_l \\ H_h \end{bmatrix} \mathbf{u}, \tag{4.5}$$

where the x-tilt, y-tilt and defocus coefficients are collected into $\mathbf{z}_l = [z_2, z_3, z_4]^T$. The SVD of H_l is

$$H_l = U_l \begin{bmatrix} \Sigma_l & \mathbf{0} \end{bmatrix} \begin{bmatrix} V_{l1}^T \\ V_{l2}^T \end{bmatrix}, \tag{4.6}$$

where Σ_l has dimensions 3×3, V_{l1} has dimensions $N_a \times 3$ and V_{l2} has dimensions $N_a \times N_p$ with $N_p = N_a - 3$. The required constraint that $\mathbf{z}_l \approx \mathbf{0}$ is enforced if we choose $\mathbf{u}$ such that $H_l\mathbf{u} = 0$. This is achieved by parametrising $\mathbf{u}$ using the columns of V_{l2}, i.e., letting $\mathbf{u} = V_{l2}\mathbf{p}$, where $\mathbf{p} \in \mathbb{R}^{N_p}$.

In summary, we have that

$$\Phi(\boldsymbol{\xi}) = \sum_{i=1}^{N_a} u_i \psi_i(\boldsymbol{\xi}), \quad \text{s.t.} \quad \mathbf{u} = V_{l2}\mathbf{p}, \tag{4.7}$$

or equivalently

$$\Phi(\boldsymbol{\xi}) = \sum_{i=1}^{N_p} p_i \omega_i(\boldsymbol{\xi}), \tag{4.8}$$

where $\omega_i(\boldsymbol{\xi})$ are the new basis functions. We have that $\omega_i(\boldsymbol{\xi}) = \sum_{j=1}^{N_a} (V_{l2})_{ji} \psi_j(\boldsymbol{\xi})$, where $(V_{l2})_{ji}$ denotes element (j, i) of V_{l2}. For a given vector $\mathbf{p}$, we can compute the control signals of the actuators with $\mathbf{u} = V_{l2}\mathbf{p}$. Similarly, for a given $\mathbf{p}$, the Zernike analysis of the induced wavefront aberration is given by $\mathbf{z} \approx HV_{l2}\mathbf{p}$.

We also applied regularisation (Hansen, 2010) by truncating the SVD of HV_{l2} to $U_1\Sigma_1V_1^T$. Using no more than 80% of the sum of the singular values, Σ_1 is a 7×7 matrix. In our experiments the deformable mirror was controlled using a vector $\mathbf{r} \in \mathbb{R}^N$ where $N = 7$. For a given $\mathbf{r}$, the control signals of the actuators of the deformable mirror are computed using $\mathbf{u} = V_{l2}V_1\mathbf{r}$. The Zernike analysis of the induced wavefront is computed using $\mathbf{z}_h \approx H_hV_{l2}V_1\mathbf{r}$ and the rms of the phase profile is given by computing the 2-norm, i.e., $\|\mathbf{z}_h\|$. This is equivalent to applying another parametrisation to (4.8). We remark that in this way, no pseudo-inverse is ever computed or used to control the deformable mirror, differently from what is done in Paterson et al. (2000), for example.

4.3 Least-squares estimation of the unknown aberration

In this section we discuss the aberration correction algorithm. In Débarre et al. (2009); Facomprez et al. (2012); Zeng et al. (2012), the authors show that, for small aberrations, the image quality metric can be modelled using a quadratic polynomial. We denote a measurement of the image quality metric at time instant k with $\tilde{y}_k$. We have that

$$\tilde{y}_k = c_0 - (\mathbf{x} + \mathbf{r}_k)^T Q(\mathbf{x} + \mathbf{r}_k) + \epsilon_k, \tag{4.9}$$

where c_0 and Q are the parameters of the quadratic polynomial. Matrix Q is a positive semidefinite matrix, i.e., $Q \succeq 0$ (Antonello et al., 2012). Vector

$\mathbf{x}$ represents the unknown aberration whereas $\mathbf{r}_k$ accounts for the aberration induced by the deformable mirror. The term ϵ_k is a placeholder that collects both the uncertainty in modelling the image quality metric and the measurement noise, and as such it cannot be measured by definition. By including this term, a measurement $\tilde{y}_k$ can be set equal to the right hand side of (4.9). Excluding ϵ_k, the right hand side of (4.9) is referred to as the approximate image quality metric in Antonello et al. (2012). The parameters c_0 and Q can be computed using the input-output measurements recorded in a calibration experiment described in section 4.4 or using the methods described in Débarre et al. (2008, 2012).

Definition of the least-squares problem

The aberration correction is achieved by maximising the image quality metric, i.e., by letting $\mathbf{r}_k = -\mathbf{x}$ in (4.9). For this reason, we must first estimate the unknown vector $\mathbf{x}$. This can be done by applying $m \geq N + 1$ trial aberrations $\mathbf{r}_1, \dots, \mathbf{r}_m$ with the deformable mirror and by taking the corresponding measurements $\tilde{y}_1, \dots, \tilde{y}_m$.

Collect $\epsilon_1, \dots, \epsilon_m$ into a vector $\boldsymbol{\epsilon}$ and $\tilde{y}_1, \dots, \tilde{y}_m$ into a vector $\tilde{\mathbf{y}}$. By stacking m instances of (4.9), we can define a vector-valued function $\mathbf{g}$

$$\mathbf{g}(\mathbf{x}) = \begin{bmatrix} c_0 - (\mathbf{x} + \mathbf{r}_1)^T Q (\mathbf{x} + \mathbf{r}_1) \\ \vdots \\ c_0 - (\mathbf{x} + \mathbf{r}_m)^T Q (\mathbf{x} + \mathbf{r}_m) \end{bmatrix}, \tag{4.10}$$

such that

$$\tilde{\mathbf{y}} = \mathbf{g}(\mathbf{x}) + \boldsymbol{\epsilon}. \tag{4.11}$$

The least-squares estimate of $\mathbf{x}$ can be obtained by minimising $\|\boldsymbol{\epsilon}\|^2$, i.e., by solving

$$\min_{\mathbf{x}} f(\mathbf{x}), \tag{4.12}$$

where

$$f(\mathbf{x}) = \|\tilde{\mathbf{y}} - \mathbf{g}(\mathbf{x})\|^2. \tag{4.13}$$

We note that if vector $\boldsymbol{\epsilon}$ follows a multivariate normal distribution with zero mean and covariance proportional to the identity matrix, solving (4.12) provides the maximum likelihood (Torrieri, 1984) estimate of $\mathbf{x}$.

Analysis of the least-squares problem

Finding the global minimum of $f(\mathbf{x})$ appears to be non trivial as $f(\mathbf{x})$ may be non-convex. This is illustrated with a two-dimensional example

in Fig. 4.1. Here, the contour plot of (4.13) is shown, when $m > N + 1$ measurements of $\tilde{y}$ are taken. The measurement noise is zero, i.e., $\boldsymbol{\epsilon} = \mathbf{0}$. Nevertheless, $f(\mathbf{x})$ is not convex and exhibits two critical points. In addition to the least-squares solution $\mathbf{x}^{\text{ls}}$ of (4.12), which is the global minimum and for which $f(\mathbf{x}^{\text{ls}}) = 0$, a local minimum $\mathbf{x}^{\text{loc}}$ is present. In case one uses $\mathbf{r}_k = -\mathbf{x}^{\text{loc}}$ to perform the aberration correction, then the residual aberration is not zero and the image quality metric is not maximised.

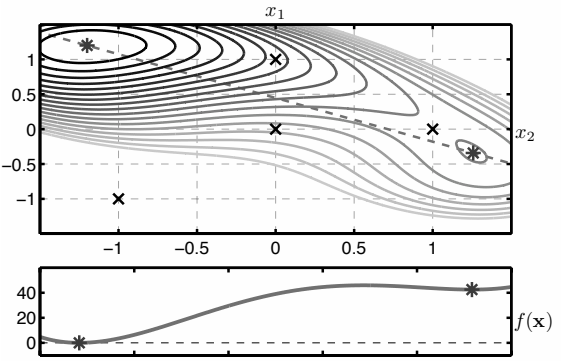

Figure 4.1: Contour plot of (4.13). In this example, $f(\mathbf{x})$ is not convex and exhibits a local minimum. The parameters are $c_0 = 100$ and $Q = \begin{bmatrix} 1.25 & 0.433 \\ 0.433 & 1.25 \end{bmatrix}$. Four measurements of $\tilde{y}$, taken at $\mathbf{r}_1 = (0,0)^T$, $\mathbf{r}_2 = (1,0)^T$, $\mathbf{r}_3 = (0,1)^T$ and $\mathbf{r}_4 = (0,1)^T$ are marked with $\times$ symbols. The global minimum $\mathbf{x}^{\text{ls}} = (-1.2, 1.2)^T$ and the local minimum $\mathbf{x}^{\text{loc}} \approx (1.2582, -0.3421)^T$ are indicated with $*$ symbols. Isolines with an elevation greater than 70 have been removed for clarity. A cross section along the dashed line is reported in the plot in the bottom.

Because the convexity property is not satisfied in general, it is unclear how $\mathbf{x}^{\text{ls}}$ can be computed. For example, a gradient based method applied to solve (4.12) may fail to compute $\mathbf{x}^{\text{ls}}$. Alternatively, more sophisticated algorithms may be unsuitable to meet the requirements of a real time implementation. Nevertheless, the global solution of (4.12) can be computed efficiently even when $f(\mathbf{x})$ is not convex, as is outlined in the following section.

Efficient computation of $\mathbf{x}^{\text{ls}}$

In Beck et al. (2008), an efficient algorithm to find the global solution of a possibly non-convex optimisation similar to (4.12) was developed, in the context of localisation problems. In this section we show how the solu-

tion proposed in Beck et al. (2008) can be applied to our problem. For the remaining part of the paper we assume that Q is strictly positive definite. This assumption is reasonable since if there are aberrations that do not affect the image quality metric then these cannot be corrected and they should be neglected during the aberration correction (Antonello et al., 2012).

Introducing an additional scalar variable α, we can reformulate (4.12) into the following equivalent constrained optimisation

$$\begin{aligned} \min_{\mathbf{x},\alpha} \sum_{k=1}^{m} \left(-\alpha - 2\mathbf{r}_k^T Q\mathbf{x} + c_0 - \mathbf{r}_k^T Q\mathbf{r}_k - \tilde{y}_k\right)^2 \\ \text{s.t.} \quad \alpha = \mathbf{x}^T Q\mathbf{x}. \end{aligned} \tag{4.14}$$

Problem (4.14) is written concisely in matrix form as

$$\min_{\mathbf{w}} \|A\mathbf{w} - \mathbf{b}\|^2 \quad \text{s.t.} \quad \mathbf{w}^T D\mathbf{w} + 2\mathbf{f}^T\mathbf{w} = 0, \tag{4.15}$$

where

$$\begin{gathered} \mathbf{w}^T = \begin{bmatrix}\mathbf{x}^T & \alpha\end{bmatrix}, R = \begin{bmatrix}\mathbf{r}_1 & \dots & \mathbf{r}_m\end{bmatrix}, \\ A = \begin{bmatrix}-2R^T Q & -\mathbf{1}\end{bmatrix}, \mathbf{b} = \begin{bmatrix}\mathbf{r}_1^T Q\mathbf{r}_1 + \tilde{y}_1 - c_0 \\ \dots \\ \mathbf{r}_m^T Q\mathbf{r}_m + \tilde{y}_m - c_0\end{bmatrix}, \\ D = \begin{bmatrix}Q & \mathbf{0} \\ \mathbf{0} & 0\end{bmatrix}, \mathbf{f}^T = \begin{bmatrix}\mathbf{0} & -1/2\end{bmatrix}^T \end{gathered} \tag{4.16}$$

and $\mathbf{1}$ and $\mathbf{0}$ denote vectors of appropriate dimensions where all components are respectively ones and zeros. The authors in Beck et al. (2008) note that (4.15) is a Generalised Trust Region Subproblem (Moré, 1993). Such problems, although non-convex in general, have necessary and sufficient optimality conditions (Moré, 1993). In particular, from Beck et al. (2008); Moré (1993), we have that $\mathbf{w}$ is a global minimiser of (4.15) if and only if there exist a Lagrange multiplier ν such that

$$\begin{aligned} (A^T A + \nu D)\mathbf{w} &= A^T\mathbf{b} - \nu\mathbf{f} \\ \mathbf{w}^T D\mathbf{w} + 2\mathbf{f}^T\mathbf{w} &= 0 \\ A^T A + \nu D &\succeq \mathbf{0}. \end{aligned} \tag{4.17}$$

We assume that matrix A is full column rank, which in turn implies that $m \geq N + 1$. This assumption on A is by no means restrictive. Because $Q \succ 0$, it can be factored $Q = V\Delta V^T$, where Δ is diagonal and full rank. Choose $R = [V, \mathbf{0}]$, where $\mathbf{0}$ is a vector of zeros, then A is full column rank.

We further assume that the optimal Lagrange multiplier ν^* is such that $A^TA + \nu^*D$ is strictly positive definite. The authors in Beck et al. (2008) point out that this more restrictive assumption could be removed with a more refined analysis. However the case where ν^* is such that $A^TA + \nu^*D$ is not strictly positive definite is unlikely to occur both in theory and in practice (Beck et al., 2008).

Under these assumptions, one can compute

$$\mathbf{w}(\nu) = (A^TA + \nu D)^{-1}(A^T\mathbf{b} - \nu\mathbf{f}) \tag{4.18}$$

for a fixed value of ν. By replacing $\mathbf{w}$ in the second equation in (4.17) with the right hand side of (4.18), one finds a univariate rational polynomial equation in ν

$$\mathbf{w}(\nu)^T D\mathbf{w}(\nu) + 2\mathbf{f}^T\mathbf{w}(\nu) = 0. \tag{4.19}$$

The optimal Lagrange multiplier ν^* can be found examining the solutions of (4.19). From the assumption $A^TA + \nu D \succ 0$, it can be derived (Moré, 1993; Beck et al., 2008) that ν must be in the interval $(I_l, +\infty)$, where $I_l = -1/\lambda_{\max}(\Delta_A^{-1/2}V_A^T D V_A \Delta_A^{-1/2})$ and we used the factorisation $A^TA = V_A\Delta_A V_A^T$. In addition, it is known (Moré, 1993; Beck et al., 2008) that (4.19) is strictly decreasing in ν within the considered interval. Therefore the desired root ν^* of (4.19) can be found efficiently, for example via a bisection algorithm (Beck et al., 2008). Once ν^* is found, the estimate of $\mathbf{x}$ is extracted from the first N components of $\mathbf{w}(\nu^*)$.

The aberration correction algorithm is therefore applied in the following manner. First the data collection step takes place, whereby the $m \geq N + 1$ trial aberrations are applied and the corresponding measurements $\tilde{y}_1, \ldots, \tilde{y}_m$ are taken. Then, ν^* is computed by finding the root of (4.19) within $(I_l, +\infty)$. The estimate $\mathbf{x}^{\text{ls}}$ of the aberration is found in the first N components of $\mathbf{w}(\nu^*)$. The aberration correction step involves applying the correction with the deformable mirror, letting $\mathbf{r} = -\mathbf{x}^{\text{ls}}$. These steps can be repeated in the following time instants by including more than m measurements to achieve a refined correction. We note that in Antonello et al. (2012), the least-squares estimate of $\mathbf{x}$ was not computed since the quadratic constraint in (4.14) was neglected to obtain a linear least-squares problem.

4.4 Experimental results

We implemented the model-based wavefront sensorless algorithm and report the experimental results in this section. Following Jesacher et al.

(2009), we employ the mean image intensity as a metric to correct aberrations in our second-harmonic microscope. Our experiments show successful aberration correction using this metric (see section 4.4).

Our first purpose is to validate a previously proposed method (Antonello et al., 2012) to compute the parameters c_0 and Q of (4.9) using input-output measurements. This validation has not been previously done in a realistic setting, since in Antonello et al. (2012) no microscope and no specimen were involved. Additionally, we intend to validate the aberration correction algorithm described in section 4.3. We report our results in the following sections.

Description of the experimental setup

A schematic of the experimental setup is shown in Fig. 4.2. The source is a Coherent Chameleon Ultra II Ti:Sa 140 fs pulsed, near-infrared laser, with a beam diameter of 1.2 mm. This beam is expanded to a 14 mm wide beam by lenses L1 and L2.

The beam is stopped down to 9.5 mm (AP) before it is reflected under an angle of about 10° by the deformable mirror (DM; Okotech, MMDM 19-channel deformable mirror). The deformable mirror is re-imaged one-to-one onto the objective back-aperture by lenses L3 and L4 (focal lengths, 300 mm). Because the deformable mirror can only introduce negative deflection, we bias the mirror so that we can apply positive and negative deflections to correct the wavefront (see Vdovin et al. (2013)). In addition, the relationship between the control signal u_i of each actuator of the deformable mirror and the voltage applied to the corresponding electrode is quadratic, so that a linear displacement of the membrane is expected (Vdovin et al., 2013). Due to this bias, the collimated beam coming from L2 is converging after being reflected by the deformable mirror. We corrected this by using lenses L4 and L3, so that a collimated beam is fed into the objective.

The sample is mounted on an xyz-piezo stage (XYZ; PI, Nanocube P-611.3S). The second-harmonic signal from the specimen is collected by the objective and split off by a 705 nm cut-off dichroic beam splitter (DBS; Semrock, FF705-Di01-25x36). This light is focused onto a 600 µm multimode fibre which is connected to a photo multiplier tube (PMT; Hamamatsu, GaAsP photocathode H7422P-40). The objective used (OBJ) is a 40×/0.9 NA Nikon air objective with spherical correction collar. We manually adjusted the collar to correct for the spherical aberration due to the cover glass and the specimen at the selected depth.

For characterisation of the deformable mirror, we interfere a tilted reference beam with a sample beam deflected off the deformable mirror to create fringes that encode the wavefront deformation. To allow this, a 50/50 beam splitter (BS1; Thorlabs, BS016) splits off part of the light into a reference arm beam, which is relayed onto the camera (CCD; AVT, Guppy Pro F-033b) by mirrors M2, M3, and M4. The sample arm beam is deflected by the deformable mirror once before flip mirror FM1 directs the light into the calibration arm. Lenses L6 and L7 re-image the deformable mirror onto a camera. For this calibration we use the alignment laser, which is a continuous wave. We used the method described in van Werkhoven et al. (2014) to decode the wavefront from the fringe patterns.

The piezo stage is controlled with a data acquisition board (National Instruments, PCI-e 6259) on a Windows computer running LabView. The deformable mirror is controlled through a PCI DAC card on a Linux computer running MATLAB and custom C code.

In the aberration correction experiments we imaged collagen fibre extracted from rat tail washed 4 times in distilled water. Following fixation in 4% paraformaldehyde, the fibre was washed in phosphate buffer saline and then embedded in 3% agarose (Sigma-Aldrich chemie GmbH) in a 35 mm glass bottom dish (MatTek Corporation). We used 900 nm excitation light to generate the second-harmonic signal.

Preparation of the experiments

We first imaged a 20×20 µm region, approximately 33 µm deep into the collagen fibre. The region is labelled with *A* in Fig. 4.3. The influence of the size of the region used for the aberration correction has been studied elsewhere (Zeng et al., 2012). For a certain setting of the deformable mirror $\mathbf{r}$, the region is scanned using the xyz stage. The corresponding value of the image quality metric $\tilde{y}$ is measured as the mean image intensity (Jesacher et al., 2009; Débarre et al., 2009; Facomprez et al., 2012; Zeng et al., 2012), i.e., the mean pixel value recorded over the region. The pixel dwell time is 0.5 ms and the sampling is 24×24 pixels. With these settings, the xyz stage does not reach the full 20 µm distance in the x scanning direction, which is the fast axis. This was not an issue since such a coarse sampling was only used to perform the aberration correction in a short time (Facomprez et al., 2012). The final images taken after the aberration correction were recorded with a higher sampling. The image deformation due to both the non-linearity and non-uniform speed of the xyz stage were removed from the final images, using interpolation and the signals recorded with the position sensors of the xyz stage.

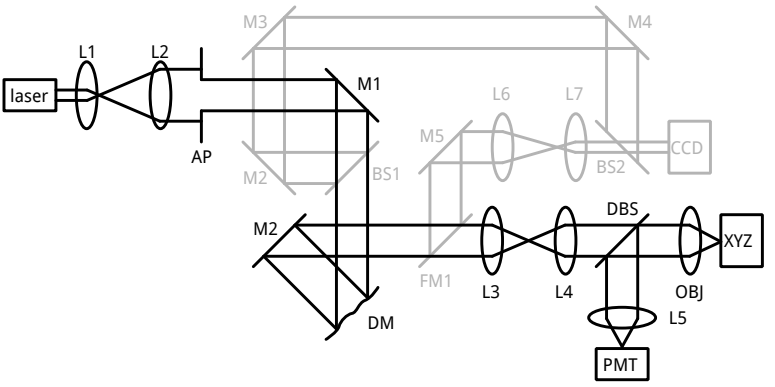

Figure 4.2: Illustration of the optical setup. The components in black are used throughout the aberration correction experiments. The components in grey are used only for the initial characterisation of the deformable mirror (DM). A pulsed laser beam is expanded with lenses L1 and L2, clipped by aperture AP and reflected by flat mirror M1 onto the DM. The DM is in an image of the back aperture of the microscope objective (OBJ), using lenses L3 and L4. The DM is illuminated under an angle of about 10° using the flat mirrors M1 and M2. The microscope objective (OBJ) focuses the light onto the specimen, which is supported by an xyz stage (XYZ). The second-harmonic signal emitted from the focal point inside the specimen is collected with the objective and separated from the illumination beam using a dichroic beam splitter (DBS). The emitted signal is focused by lens L5 onto a photo multiplier tube (PMT). For characterising the DM, the surface of the DM is re-imaged onto a CCD camera (CCD) using the flip mirror FM1, flat mirror M5 and lenses L6 and L7. A reference arm is created using beam splitter BS1, flat mirrors M2, M3, M4 and beam splitter BS2. A coherence-gated fringe analysis method described elsewhere van Werkhoven et al. (2012, 2014) is applied to the fringe pattern generated onto CCD.

First, the static aberrations in the system due to misalignment and imperfections in the optical components were corrected. We used the non-zero initial aberration that was found during the calibration of the deformable mirror in section 4.2 (about 0.79 rms rad at 900 nm, mostly astigmatism). At this point the Nelder–Mead algorithm (Lagarias et al., 1998) was executed four times to find a value $\mathbf{r}$ that maximises $\tilde{y}$. Unfortunately, this led to the saturation of two actuators, indicating that the stroke of the deformable mirror may be insufficient for completely suppressing the aberration in this region. We selected a slightly sub-optimal vector $\mathbf{r}$ from the vectors generated by the Nelder–Mead algorithm. For the selected vector, the maximum normalised voltage of the actuators was 0.72, i.e., $\|\mathbf{u}\|_\infty \leq 0.72$, $\tilde{y}$ improved by 3% and a total aberration of about 0.18 rms rad

was suppressed. We used this state as the new initial condition for the rest of the experiments, i.e., $\mathbf{r} = \mathbf{0}$ is mapped to this setting of the deformable mirror. In the following sections, all the units in rad are referenced to the 900 nm excitation laser light.

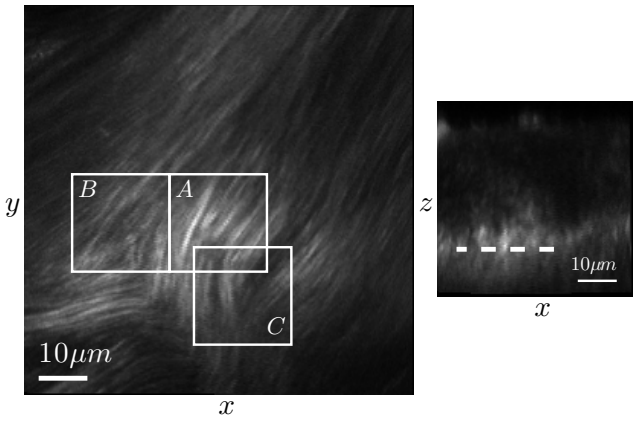

Figure 4.3: Cross sections of rat tail collagen fibre used in our experiments. The smaller image on the right hand side is an xz cross section (50 × 50 µm, 128 × 128 pixels). The dashed line denotes an xy cross section (80 × 80 µm, 256 × 256 pixels) approximately 33 μm deep, which is shown on the left hand side. Three different 20 × 20 µm regions are marked.

Computation of the parameters of the quadratic polynomial using input-output measurements

We executed the computation of the parameters of the quadratic polynomial used for modelling the image quality metric multiple times. Each time, the sequence of input vectors consisted of two sub-sequences. The first subsequence contained random vectors $\mathbf{r}_1$, ..., $\mathbf{r}_{250}$ and was used for the validation and the cross-validation. The second subsequence contained 70 fixed vectors (each vector having a single non zero component). The second subsequence was included because the 250 random vectors may be insufficient to uniformly sample the N-dimensional space of the inputs. In Antonello et al. (2012) 3750 random vectors were used, but this was impractical here, due to the time necessary to move the xyz stage. The maximum rms rad of the input aberrations did not exceed 0.81. This value was empirically tuned by examining the goodness of fit as a function of the the maximum rms (Antonello et al., 2012).

For each input vector in the sequence, we measured the corresponding output of $\tilde{y}$. The resulting input-output data, i.e., collections $\tilde{y}_1$, ..., $\tilde{y}_{320}$ and $\mathbf{r}_1$, ..., $\mathbf{r}_{320}$ were used to formulate the following optimisation problem (Antonello et al., 2012)

$$\begin{aligned}
&\min_{\tilde{\mathbf{x}}} \|\tilde{A}\tilde{\mathbf{x}} - \tilde{b}\| \quad \text{s.t.} \\
&\tilde{A} = \begin{bmatrix} 1 & \mathbf{r}_1^T & -\mathbf{r}_1^T \otimes \mathbf{r}_1^T \\ \vdots & \vdots & \vdots \\ 1 & \mathbf{r}_{320}^T & -\mathbf{r}_{320}^T \otimes \mathbf{r}_{320}^T \end{bmatrix}, \\
&\tilde{b} = \begin{bmatrix} \tilde{y}_1 & \dots & \tilde{y}_{320} \end{bmatrix}^T, \\
&\tilde{\mathbf{x}} = \begin{bmatrix} c_0 & \mathbf{c}_1^T & \mathrm{vec}(Q)^T \end{bmatrix}^T, \\
&\quad Q \succeq 0,
\end{aligned} \tag{4.20}$$

where vec(·) denotes the vectorisation operation and $\otimes$ the Kronecker product. This programme was solved using CVXOPT (Andersen et al., 2013) (see Andersen et al. (2011) for further details).

Validation and cross-validation of the computed parameters

The results of applying (4.20) in region A marked in Fig. 4.3 are shown in Fig. 4.4. The computation of the parameters was repeated six times. Each time, a new input-output data set was acquired, $\mathcal{D}_1$, ..., $\mathcal{D}_6$. For each input-output data set, optimisation (4.20) was solved generating six sets of parameters, each set comprising c_0, $\mathbf{c}_1$ and Q. The sets are denoted as $\mathcal{M}_1$, ..., $\mathcal{M}_6$. We quantified the goodness of fit for all combinations of $\mathcal{D}$ and $\mathcal{M}$ by means of the $\mathcal{R}^2$ indicator. Using the random input subsequence of $\mathcal{D}_i$ and $\mathcal{M}_j$, we computed the predicted output $\hat{\mathbf{o}} \in \mathbb{R}^{250}$ of the image quality metric. The input-output data points obtained from the deterministic input subsequence of 70 vectors were discarded and not included in the computation of the $\mathcal{R}^2$ indicator. The following equations were employed for the $\mathcal{R}^2$ indicator,

$$\begin{aligned}
&\mathcal{R}^2 = 1 - S_r/S_t, \qquad S_r = \|\mathbf{o} - \hat{\mathbf{o}}\|^2, \\
&S_t = \|\mathbf{o} - \bar{o}\mathbf{1}\|^2, \quad \bar{o} = (1/250)\mathbf{1}^T\mathbf{o},
\end{aligned} \tag{4.21}$$

where $\mathbf{o}$ is the measured output of $\mathcal{D}_i$. An $\mathcal{R}^2 = 1$ implies a perfect fit of the experimental data.

Fig. 4.4 reports $\mathcal{R}^2$ indicators that are close to one, implying a good fit of the experimental data. A good fit is also found for the combinations that are off the main diagonal. Here the parameters c_0, $\mathbf{c}_1$ and Q allow to accurately predict cross validation output data. Similar results were found for the other two regions marked in Fig. 4.3.

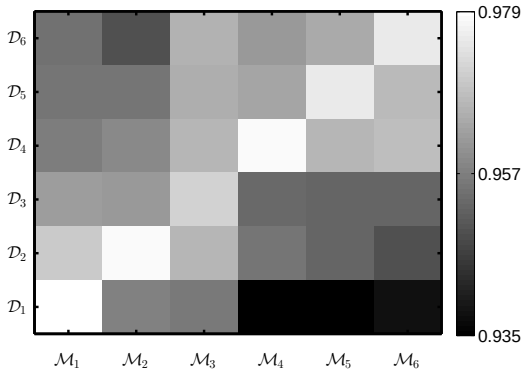

Figure 4.4: Validations and cross validations of the computation of c_0, $\mathbf{c}_1$ and Q using (4.20). The computation has been performed 6 times in region A in Fig. 4.3. $\mathcal{D}_i$ denotes the input-output data taken during the i-th time. $\mathcal{M}_i$ denotes the set of parameters (c_0, $\mathbf{c}_1$ and Q in (4.20)) computed from $\mathcal{D}_i$. For each combination $\mathcal{M}_i$ and $\mathcal{D}_j$, the i-th random input subsequence and $\mathcal{M}_j$ are used to compute the predicted output $\hat{\mathbf{o}} \in \mathbb{R}^{250}$. Each rectangle reports the goodness of fit ($\mathcal{R}^2$, see (4.21)) computed comparing $\hat{\mathbf{o}}$ with the corresponding measured output $\mathbf{o} \in \mathbb{R}^{250}$ of $\mathcal{D}_j$. A value of one for the goodness of fit indicates that the model fits the data without error. High values of the goodness of fit are reported in all combinations showing that (4.20) is a robust method to compute the parameters.

Correction of the residual aberration

In this section we apply the aberration correction algorithm described in section 4.3. First, we attempt to further reduce the residual aberration in region A, which is marked in Fig. 4.3. Some aberration may not have been completely suppressed by the Nelder–Mead algorithm, which was applied to region A in section 4.4. We therefore expect no improvement or a small improvement in region A. Second, we also apply the aberration correction to regions B and C, where the Nelder–Mead algorithm was not applied. Here we expect some improvement, provided that the aberrations found in regions B and in C are different from the aberration found in region A.

We take the parameters c_0, $\mathbf{c}_1$ and Q that were computed using $\mathcal{D}_6$ in section 4.4. In order to apply the algorithm, the following modified parameters need to be used, i.e., $c_0' = c_0 + (1/4)\mathbf{c}_1^T Q^{-1}\mathbf{c}_1$, $\mathbf{c}_1' = \mathbf{0}$ and $Q' = Q$. This modification is necessary since, for simplicity, in section 4.3 we neglected the linear term $\mathbf{c}_1$. This term corresponds to the aberration that is present when computing the parameters of the quadratic polynomial, (see Antonello et al. (2012) for more details). The aberration correction ex-

periment is applied in the three regions using the corresponding parameters for each region. A summary of the results is given in Fig. 4.5.

In Fig. 4.5a, the normalised measurements of the image quality metric are reported for region A (curve with $\circ$ markers), region B (curve with $\square$ markers) and region C (curve with $\star$ markers). The measurements are normalised using the corresponding maximum recorded measurement $\tilde{y}_{\max}$ in each region. The initial value of $\tilde{y}$ is reported at sample time $k = 0$. This measurement is not supplied to the aberration correction algorithm. The data collection step is performed between time $k = 1$ and $k = 8$ inclusive, where $N + 1 = 8$ trial aberrations are applied. From time $k = 9$ onwards, the aberration correction step is applied.

Marginal improvement is found in region A (curve with $\circ$ markers) and B (curve with $\square$ markers), where aberrations of about 0.38 and 0.37 rms rad are corrected. The rms of each aberration is estimated using $\|H_h V_{l2} V_1 \mathbf{x}^{\text{ls}}\|$, adjusted for the 900 nm excitation light. In region C, (curve with $\star$ markers) an estimated 1.27 rms rad aberration is corrected, leading to an improvement of 20% of the image quality metric. Nevertheless, two actuators of the deformable mirror were saturated.

Two 256×256 pixels images of region C are reported in Fig. 4.5b and Fig. 4.5c. These images are recorded before ($k = 0$, Fig. 4.5b) and after ($k = 24$, Fig. 4.5c) the aberration correction. The cross sections marked in the images are reported in a single graph in Fig. 4.5d. The image taken at time $k = 24$ is 18% brighter and shows finer detail in the bottom and right parts. Here some structure of the fibre was not visible at time $k = 0$. The improvement is less clear when examining the left and top parts of the region. One possible reason for the variability of the improvement is that the aberration is not spatially invariant over the considered field of view. Finally, we note that the applied correction was not optimal since two actuators of the deformable mirror were saturated. We conclude by observing that this improvement after the aberration correction is compatible with what was achieved by running four iterations of the Nelder–Mead algorithm in section 4.4.

Validation of the aberration correction algorithm

To assess whether the aberration correction algorithm is effectively removing aberration we performed a different kind of experiment. First we introduce a known amount of aberration using the deformable mirror. We then apply the aberration correction algorithm to suppress this aberration. The algorithm is not supplied with any information about the known aberration. Finally we evaluate the residual aberration by com-

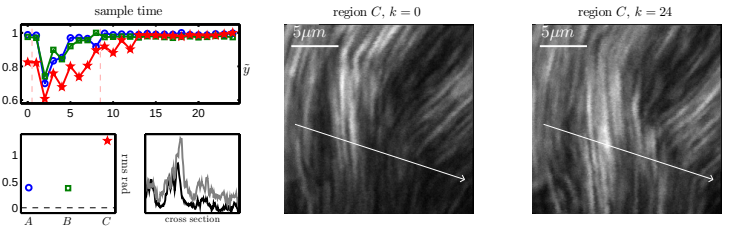

Figure 4.5: Summary of three aberration correction experiments. (a) evolution of the normalised image quality metric. The experiments were performed in region A (curve with $\circ$ markers), B (curve with $\square$ markers) and C (curve with $\star$ markers), which are marked in Fig. 4.3. For each region, the corresponding parameters computed by solving (4.20) were used. $\tilde{y}_{\max}$ is the maximum measurement of $\tilde{y}$ in each region. The estimated rms rad of each aberration is 0.38 for region A, 0.37 for region B and 1.27 for region C. (b) 256×256 pixels image of region C at sample time $k = 0$. (c) 256×256 pixels image of region C at sample time $k = 24$. (d) cross sections taken along the arrows marked in (b) and (c), black for (b) and grey for (c).

paring the estimate of the aberration provided by the algorithm with the known aberration. This kind of experiment is commonly employed in the literature to assess the effectiveness of the aberration correction (Débarre et al., 2007; Facomprez et al., 2012; Zeng et al., 2012; Antonello et al., 2012).

Fig. 4.6 reports a summary of the correction of 20 random aberrations introduced with the deformable mirror in region A. The upper plot in Fig. 4.6 shows some statistical indicators of the normalised measurements of the image quality metric. The measurements have been normalised using the maximum measurement of the metric $\tilde{y}_{\max}$ that is recorded throughout the 20 experiments. The median, 25th and 75th percentiles are computed in each time instant, see the caption of Fig. 4.6 for a detailed legend. The same analysis has been made for the residual aberration and is reported in the lower plot in Fig. 4.6. The rms of the residual aberration is computed as the rms of the difference between the known aberration introduced by the deformable mirror and the respective estimate provided by the algorithm. From this figure, we conclude that the image quality metric is consistently maximised, as the median is close to 1 after the aberration correction is applied from sample time $k = 9$ onwards. This is consistent with the reduction in the residual aberration reported in the lower plot.

The same experiments were performed in region B and C. In both cases we used the corresponding modified parameters, computed using $\mathcal{D}_6$ in section 4.4. The results are reported in Fig. 4.7 and Fig. 4.8. Whereas the

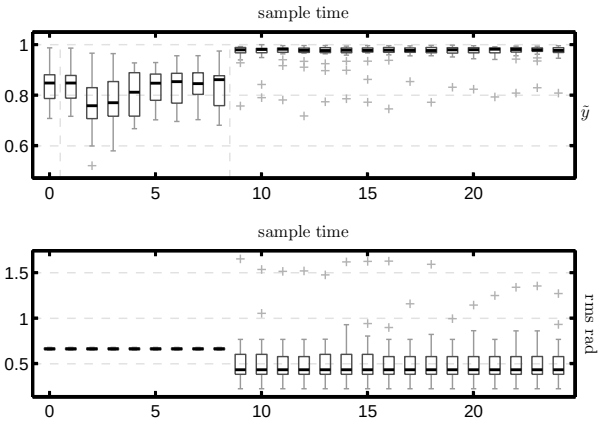

Figure 4.6: Summary of the correction of 20 random aberrations induced by the deformable mirror in region A, which is marked in Fig. 4.3. The upper plot reports the normalised measurements of the image quality metric. The measurements are normalised using the maximum measurement $\tilde{y}_{\max}$ that is recorded throughout the 20 experiments. At time $k = 0$ the initial value of $\tilde{y}$ is reported, this data point is not supplied to the aberration correction algorithm. Between time $k = 1$ and $k = 8$, the data collection step is executed. From time $k = 9$ onwards, the aberration correction step is applied. A statistical analysis is made at each time instant using the function `boxplot` from MATLAB. The tops and bottoms of the rectangles denote the 25th and 75th percentiles, the horizontal lines in the middle of the rectangles denote the medians, the whiskers extend to the furthest measurements not considered as outliers. The + symbols denote single outliers. The same statistical analysis is performed for the residual aberration and the results are shown in the lower plot.

results for region C are similar to the results obtained in region A, the results in region B do not show a good performance, since the medians of the residual aberration are comparable with the initial aberration before the correction.

Out of the 20 trials in region B, we report respectively the ones that resulted in the maximum and in the minimum improvement of $\tilde{y}$ in Fig. 4.9. In Fig. 4.9a, some fine structure of the fibre is more visible after the correction, which is compatible with a successful aberration correction. On the other hand, in Fig. 4.9b, the aberration correction failed, as both the image after the correction is visually worse and the intensity is slightly decreased.

The experiments resulting in the maximum and in the minimum improvement of $\tilde{y}$ in region C are also reported in Fig 4.10. In Fig 4.10a, a successful

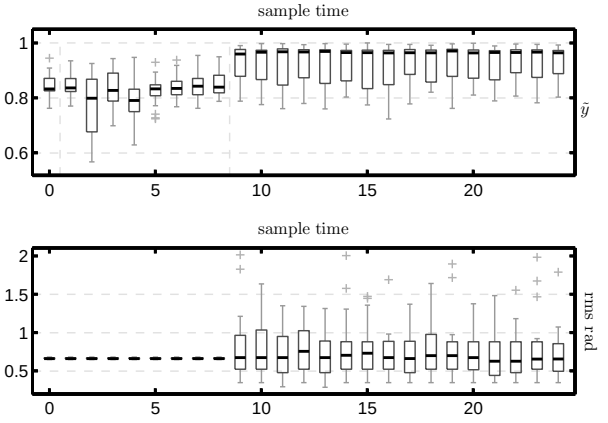

Figure 4.7: Summary of the correction of 20 random aberrations induced by the deformable mirror in region B. See the caption of Fig. 4.6 for a legend of the plots.

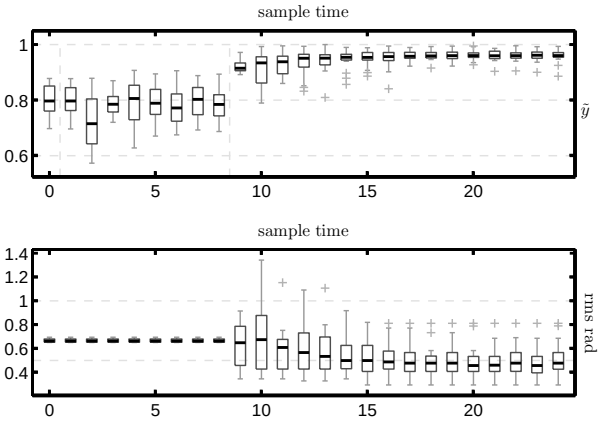

Figure 4.8: Summary of the correction of 20 random aberrations induced by the deformable mirror in region C. See the caption of Fig. 4.6 for a legend of the plots.

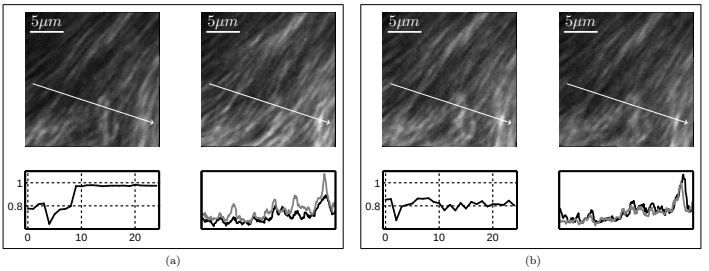

Figure 4.9: Two aberration correction experiments from the set of experiments reported in Fig. 4.7. These two experiments resulted respectively in the maximum (a) and the minimum (b) improvement of $\tilde{y}$. Both in (a) and (b), a 256×256 pixels image is taken before (on the left, $k = 0$) and after (on the right, $k = 24$) the aberration correction. The graphs in the bottom of (a) and (b) show respectively the evolution of the normalised metric (on the left) and the cross sections indicated by the arrows in the images (on the right). In the cross section graphs, the dark and the light lines correspond respectively to $k = 0$ and $k = 24$.

aberration correction is shown, with a clear maximisation of $\tilde{y}$ and a noticeable improvement in the contrast of the image after the correction. In Fig 4.10b, the improvement is more marginal.

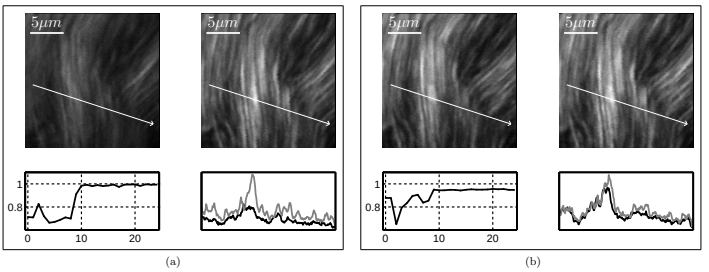

Figure 4.10: Two aberration correction experiments from the set of experiments reported in Fig. 4.8. These two experiments resulted respectively in the maximum (a) and the minimum (b) improvement of $\tilde{y}$. Refer to the caption of Fig. 4.9 for a detailed legend.

Analysis of the experimental results

We computed the correlation among different quantities to concisely assess the results of the 60 aberration correction experiments reported in

Fig. 4.6, Fig. 4.7 and Fig. 4.8. Considering the last time instant $k = 24$, we set up a saturation indicator variable $s_1, ..., s_{60}$ that is 1 if saturation of some actuators of the deformable mirror occurred and -1 otherwise.

We computed a correlation of -0.2477 between the normalised measurement of the image quality metric and the saturation indicator variable. These two quantities are slightly inversely correlated, meaning that saturation of some actuators negatively affected the final value of the image quality metric. The correlation between the final rms of the residual aberration and the saturation indicator variable was 0.3457. This positive correlation shows that a larger amount of residual aberration was found when the stroke of the deformable mirror was exhausted. Finally we computed a correlation of -0.7388 between the normalised measurement of the image quality metric and the rms of the residual aberration, which confirms that some aberration is removed by maximising the image quality metric. We conclude that saturation of the deformable mirror was an issue that hampered the results in our experimental validation.

Variations of the parameters over the field of view

We report spatial variations in the parameters c_0, $\mathbf{c}_1$ and Q. The parameters differed when computed respectively in region A, B and C in Fig. 4.3. Due to the variations, we were not able to apply the aberration correction algorithm using a single set of parameters, e.g., by correcting aberrations in region B and C using the parameters computed from region A. Variations in the parameters represent a challenge for model-based aberration correction algorithms, since the parameters are computed once only with a calibration experiment (Neil et al., 2000; Booth et al., 2002; Booth, 2006; Débarre et al., 2007; Booth, 2007b; Débarre et al., 2008, 2009; Jesacher et al., 2009; Song et al., 2010; Linhai & Rao, 2011; Facomprez et al., 2012; Zeng et al., 2012; Antonello et al., 2012).

Parameter $\mathbf{c}_1$ depends on the non-zero aberration that is present when collecting the input-output measurements used in (4.20). This parameter can be removed by applying the aberration correction algorithm as done in section 4.4. Instead, c_0 is dependent on the maximum value of the image quality metric, which differed in the three regions. We found variations in Q. For example, the largest eigenvalue of Q varied by about 30% in region B and by about 22% in region C with respect to its value in region A. The eigenvectors of Q were also affected. For instance, the eigenvector corresponding to the second largest eigenvalue of Q was rotated by about 7° in region B and by about 21° degrees in region C with respect to its orientation in region A.

We note that when using the algorithms discussed in Facomprez et al. (2012), the eigenvalues of Q are computed from scratch each time the aberration correction is applied (see section 4 in Antonello et al. (2012)). This is possible by applying at least $2N + 1$ trial aberrations and by approximating the solution of (4.12). Nevertheless, also these algorithms do not account for possible variations in the orientation of the eigenvectors, as found in our experiments. These variations affect the performance of the aberration correction, as investigated in section 3 in Facomprez et al. (2012). Therefore updating the parameters of the model as different regions of the specimen are acquired is an open research challenge.

4.5 Conclusion

In this paper we present a procedure to define a new set of basis functions for the control of the deformable mirror. The new basis functions can be made approximately orthogonal to a set of Zernike modes. This is necessary for applying aberration correction in scanning microscopy applications, where the deformable mirror must not induce the x-tilt, y-tilt and defocus aberrations.

The second contribution concerns the algorithm used for the aberration correction. We consider computing the least-squares estimate of the unknown aberration. Although this problem is non-convex in general, the least-squares estimate can be computed efficiently by exploiting results already applied in the solution of localisation problems (Beck et al., 2008). Once the least-squares estimate is computed, the aberration correction is applied by maximising the image quality metric.

We implement the aberration correction algorithm in a second-harmonic microscope. First we validate a previously proposed (Antonello et al., 2012) method to compute the parameters of the quadratic polynomial used to model the image quality metric directly from input-output measurements. Second, we validate the aberration correction algorithm discussed in this paper. We also report the measurement of variations in the parameters of the quadratic polynomial over the field of view.

Acknowledgements

This research is supported by the Technology Foundation STW under project number 10433 that is part of the Smart Optics Systems perspective programme directed by Prof. M. Verhaegen.